

## Revision 1

1  
2  
3  
4  
5  
6  
7  
8  
9  
10  
11  
12  
13  
14  
15  
16  
17  
18  
19  
20  
21  
22  
23  
24  
25  
26  
27  
28  
29

# **Kinetics of antigorite dehydration: a trigger for lower-plane seismicity in subduction zones**

Tao Liu<sup>1</sup>, Duojun Wang<sup>1</sup>, Kewei Shen<sup>1</sup>, Chuanjiang Liu<sup>1</sup>, Li Yi<sup>2</sup>

1. Key Laboratory of Computational Geodynamics, College of Earth and Planetary Sciences, University of Chinese Academy of Sciences, Beijing 100049, China

2. Institute of Earthquake Forecasting, China Earthquake Administration, Beijing, China

Corresponding author email: [duojunwang@ucas.ac.cn](mailto:duojunwang@ucas.ac.cn) (D. Wang)  
[yili@cea-ies.ac.cn](mailto:yili@cea-ies.ac.cn) (L. Yi)

30

31

32

33

## Abstract

34

35

36

37

38

39

40

41

42

43

44

45

46

47

48

49

50

51

Antigorite dehydration experiments were performed under ambient pressure using a non-isothermal thermogravimetric analysis. Antigorite, with a grain size of 5-10  $\mu\text{m}$ , was analyzed using heating rates of 10, 15, 20, and 25  $\text{K} \cdot \text{min}^{-1}$  at temperatures of up to 1260 K. The results show that the progress of the dehydration reaction varies with the heating rate, and the dehydration reaction of antigorite occurs within a temperature range of 800-1050 K. Several models were used to fit the dehydration results, and the double-Gaussian distribution activation energy model (2-DAEM) yielded the best fit to the experimental data. The dehydration kinetics of antigorite follow 2-DAEM, and there is a compensation effect between the pre-exponential factor and the average activation energy. The activation energy of the first step of antigorite dehydration stretches out a wide interval, the second step has a significantly higher activation energy, distributed on a narrower interval. We determined that the release rate of  $\text{H}_2\text{O}$  is  $8.0 \times 10^{-5}$  and  $2.1 \times 10^{-3} m_{fluid}^3 m_{rock}^{-3} \text{s}^{-1}$  at 893 K and 973 K, respectively, which are near the onset temperature for the isothermal dehydration reaction. Our results indicate that antigorite dehydration is fast enough to induce mechanical instabilities that may trigger seismicity in the lower plane of the double seismic zone.

52

## 53 **Introduction**

54 In subduction zones aqueous fluids released during the dehydration of hydrous  
55 minerals leads to metasomatism and partial melting in the overlying mantle (e.g.  
56 Scambelluri et al. 2001), which, in turn, induces magmatism (e.g. Hattori and Guillot  
57 2003; Peacock and Wang 1999; Ulmer and Trommsdorff 1995) and triggers  
58 earthquakes (e.g. Hacker et al. 2003; Jung et al. 2004; Okazaki and Hirth 2016;  
59 Peacock 2001; Yamasaki and Seno 2003). In particular, earthquakes occurring at  
60 intermediate depths (50-200 km) in double seismic zones (DSZ; Yamasaki and Seno  
61 2003) comprising upper and lower Wadati-Benioff planes may be related to  
62 dehydration (Ferrand et al. 2017; Hacker et al. 2003; Incel et al. 2017; Peacock 2001).  
63 The dehydration process in subducting oceanic slabs induces several geophysical  
64 anomalies including low seismic velocity (Ferrand et al. 2017; Hacker et al. 2003;  
65 Jung et al. 2004; Peacock 2001; Yamasaki and Seno 2003) and high conductivity  
66 anomalies (Soyer and Unsworth 2006; Wang et al. 2017; Worzewski et al. 2010).

67 Recent publications have directly addressed antigorite dehydration and its  
68 implications for the seismicity of subducting mantle (e.g. Ferrand et al. 2017; Gasc et  
69 al. 2017). Several experiments have shown that antigorite dehydration is not “seismic”  
70 (Chernak and Hirth 2010, 2011; Gasc et al. 2017; Okazaki and Hirth 2016).  
71 Particularly, it was found that, using a ratio of heating rate to strain rate that is typical  
72 for actual subducting slabs (100-1000 K), antigorite samples deform aseismically  
73 (Chernak and Hirth 2011; Gasc et al. 2017; 2011), whereas antigorite-olivine mixtures

74 undergo seismic events (Ferrand et al. 2017). Most likely, a dehydration-driven stress  
75 transfer (DDST) triggers earthquakes in fresh peridotite at the tip of dehydrating faults  
76 (Ferrand et al. 2017), as supported by recent field observations (Ferrand et al. 2018;  
77 Plümper et al. 2016; Scambelluri et al. 2017). Ferrand et al. (2017) experimentally  
78 demonstrated that intermediate-depth earthquakes, particularly those of the lower  
79 Wadati-Benioff planes (LWBP), are triggered by the dehydration of very limited  
80 amounts of antigorite, both for  $> 0$  and  $< 0$  volume changes, which means that these  
81 earthquakes are not a result of aqueous fluid overpressure. Nonetheless, the role of  
82 released aqueous fluid by antigorite still needs to be investigated.

83         Serpentine minerals are the most abundant hydrous minerals in altered  
84 ultramafic rocks (Hyndman and Peacock 2003) and contain up to approximately 13 wt%  
85 H<sub>2</sub>O (Schmidt and Poli 1998). Serpentine has three main varieties: lizardite, chrysotile  
86 and antigorite (Ulmer and Trommsdorff 1995). Antigorite is the only serpentine  
87 mineral stable above temperatures of  $\sim 875$  K in subduction zones (Reynard et al.  
88 2007; Shao et al. 2014). Several studies have considered that the limit of the antigorite  
89 stability field is near an isotherm that fits the lower plane earthquake hypocenters (e.g.  
90 Abers et al. 2013; Peacock 2001; Yamasaki and Seno 2003), i.e., between 1 and 5 GPa.  
91 Therefore, antigorite dehydration has been regarded as a candidate to explain the  
92 seismicity of the lower plane of the double seismic zone (Dobson et al. 2002; Hilairet  
93 et al. 2007; Omori et al. 2004; Peacock 2001).

94         The dehydration of serpentine minerals has been the subject of many previous  
95 studies (Eggler and Ehmman 2010; Gualtieri et al. 2012; Trittschack and Grobéty 2012;

96 Viti 2010). Recently, synchrotron HP experiments with acoustic recordings (Ferrand  
97 et al. 2017) have demonstrated that antigorite dehydration leads to peridotite  
98 embrittlement through a stress transfer from dehydrating serpentinized faults to fresh  
99 peridotite volumes. However, the kinetics of antigorite dehydration still requires  
100 investigations. Previously, antigorite dehydration was investigated using  
101 time-resolved X-ray diffraction (Chollet et al. 2011; Gualtieri et al. 2012; Perrillat et  
102 al. 2005), high-temperature infrared microspectroscopy (Sawai et al. 2013) and  
103 thermogravimetric analysis (Pérez-Rodríguez et al. 2005; Viti 2010; Weber and Greer  
104 1965). These studies have led to quite different conclusions. Dehydration is controlled  
105 by surface growth processes at the edges of grains, as shown by X-ray diffraction  
106 (Perrillat et al. 2005); in contrast, the one-dimensional diffusion process matches well  
107 with the experimental data using in situ high-temperature infrared microspectroscopy,  
108 which enables the water species to be distinguished (Sawai et al. 2013). A recent  
109 thermogravimetric analysis using three heating rates shows that the dehydration  
110 kinetics follow a three-dimensional phase boundary reaction model (Balucan et al.  
111 2011).

112 In addition, most previous studies of antigorite dehydration kinetics have used  
113 isothermal methods. Isothermal methods have some disadvantages that can be  
114 overcome by non-isothermal methods. For example, non-isothermal methods can  
115 determine changes in the activation energy as the reaction progresses. Each change  
116 indicates that either the contribution of an individual parallel step changes or that a  
117 new reaction step contributes to the overall rate (Trittschack and Grobéty 2012;

118 Vyazovkin and Wight 1997; Wang et al. 2015).

119 In this work, our goal was to study the kinetics of antigorite dehydration  
120 using non-isothermal experiments to determine the best kinetic model and therefore to  
121 understand the constraints on the fluid production rate resulting from serpentine  
122 dehydration, which, in turn, should impact intermediate-depth seismicity in  
123 subduction zones.

124

## 125 **Experimental Procedure**

### 126 **Sample Preparation**

127 Antigorite starting material was collected from the Nagasaki metamorphic belt  
128 in Japan. The pure antigorite crystals were picked to serve as samples. The chemical  
129 composition of this material was analyzed using an Electron Probe MicroAnalyzer  
130 (EPMA) (JXA-8230 at HeFei University of Technology). The chemical composition  
131 of the sample is  $Mg_{2.75}Fe_{0.09}Al_{0.06}Si_{2.03}O_5(OH)_4$  (see detail in **Table S1** ), which was  
132 also presented by Wang et al. (2017). The pure antigorite crystals were crushed and  
133 ground to obtain powder. Various grain size fractions were separated from the  
134 powdered material according to Stokes's law. Particles with diameters ranging from 5  
135 to 10  $\mu m$  were selected and stored above 423 K in a vacuum oven for one week,  
136 eliminating absorbed molecular  $H_2O$ .

### 137 **Experimental methods**

#### 138 **Dehydration experiments**

139 The dehydration experiments were performed using thermogravimetric (TG)

140 analysis with a Q600 SDT device at Peking University. Non-isothermal runs were  
141 monitored to study antigorite dehydration with heating rates of 10, 15, 20, and 25  
142  $\text{K} \cdot \text{min}^{-1}$ . The powdered samples were placed in corundum sample holders. The  
143 sample weights for the non-isothermal experiments were 5.055, 5.024, 5.059 and  
144 5.072 mg, respectively. The samples were heated in an N<sub>2</sub> inert atmosphere up to a  
145 temperature of 1260 K. The data were collected at an interval of 1 second.

### 146 **First-principle calculations**

147 Our first-principle calculations were performed with CASTEP (Clark 2005) codes  
148 based on the plane wave basis set, the norm-conserving pseudopotentials (Hamann et  
149 al. 1979; Lin et al. 1993) for electron-ion interaction and the local density  
150 approximation (LDA) for the exchange-correlation interaction. The Brillouin zones  
151 were sampled using the  $\Gamma$ -point for antigorite. The cut-off energy was set to 500 eV,  
152 and the SCF tolerance was  $5 \times 10^{-7} \text{ eV} \cdot \text{atom}^{-1}$ .

153

### 154 **Kinetic models**

155 To describe the dehydration progress under non-isothermal conditions, the  
156 mass fraction of the released volatiles ( $\alpha$ ) is defined as:

$$157 \quad \alpha = \frac{m_0 - m_T}{m_0 - m_f} \quad (1)$$

158 where  $m_0$ ,  $m_T$  and  $m_f$  are the initial mass, the mass at temperature  $T$  and the final  
159 mass of the sample, respectively.

160 The general rate equation for a non-isotherm reaction is:

$$161 \quad \frac{d\alpha}{dT} = \frac{kf(\alpha)}{\beta} \quad (2)$$

162 where  $f(\alpha)$  is a mechanism function,  $\beta = \frac{dT}{dt}$  is the heating rate,  $k$  is the rate  
163 constant defined as:

$$164 \quad k = A \exp\left(-\frac{E}{RT}\right) \quad (3)$$

165 Combining **Eq. 2** and **Eq. 3**, an integrated form of the general rate equation for a  
166 non-isothermal reaction is shown below (Ozawa 1965; Wang et al. 2015).

$$167 \quad G(\alpha) = \int_0^\alpha \frac{d(\alpha)}{f(\alpha)} = \frac{A}{\beta} \int_0^T \exp\left(-\frac{E}{RT}\right) dT \quad (4)$$

168 where  $G(\alpha)$  is a mechanism function with an integrated form,  $E$  is the apparent  
169 activation energy, and  $R$  is the gas constant. The apparent activation energy is  
170 calculated using the Flynn-Wall-Ozawa (FWO) method (Flynn and Wall 1967; Ozawa  
171 1965, 1986), which is expressed as:

$$\ln\beta = \ln\frac{AE}{RG(\alpha)} - 5.3308 - 1.052\frac{E}{RT} \quad (5)$$

172

## 173 **Results and Discussion**

174 **Fig. 1** shows the thermogravimetric data for natural antigorite with heating rates  
175 of 10, 15, 20, and 25 K · min<sup>-1</sup>. The peak temperature of antigorite dehydration  
176 increases with increasing heating rate. The dehydration trend of talc shows similar  
177 behavior (Wang et al. 2015). Antigorite dehydration is observed within the  
178 temperature range of 800 K to 1050 K. The average weight loss is as high as 12.75  
179 wt%, which is in agreement with the theoretical structural water content of antigorite  
180 of ~13 wt% (Mellini et al. 1987; Uehara 1998), and the heating rate does not affect  
181 the mass loss.

182 The activation energy derived from the FWO method changes from 130 to 400



183  $\text{kJ} \cdot \text{mol}^{-1}$  as shown in **Fig. 2**. The apparent activation energy increases as the  
184 reaction progresses in our experiments. We analyzed the non-isothermal kinetic data  
185 using the  $n$ -th order reaction. The  $n$ -th order reaction integral forms are as follows  
186 (Ozawa 1970):

$$G(\alpha) = \frac{(1 - (1 - \alpha)^{1-n})}{1 - n} \quad n \neq 1 \quad (6)$$

187 The fitting parameters and errors are listed in **Table 1**. The best-fit value of  $n$   
188 is 2.2. However, the 2.2-order model cannot fit the data well, indicating that our  
189 experimental data cannot be interpreted by the  $n$ -th order reactions, particularly within  
190 the temperature range of 800-950 K as shown in **Fig. 3**. A problem arises: the  
191 apparent activation energy ( $E$ ) is a fixed value in the  $n$ -th reactions, but still the  
192 activation energy of antigorite dehydration determined via the FWO method  
193 fluctuates substantially as shown in **Fig. 2**. Antigorite dehydration may consist of  
194 several parallel reactions. Therefore, we attempt to find a new model to describe  
195 antigorite dehydration using a double-Gaussian distribution activation energy model  
196 (2-DAEM).

197 The distribution activation energy model (DAEM) assumes that the  
198 dehydration mechanism uses an infinite number of irreversible, independent, parallel  
199 reactions of different activation energies that reflect variations in the bond strengths of  
200 the species (Cai et al. 2014; Navarro et al. 2008; Várhegyi et al. 2011; Zhang et al.  
201 2014). The different activation energies are represented by a continuous distribution  
202 function. The double-Gaussian distributed activation energy model (2-DAEM) is  
203 based on the assumption that two sets of parallel reactions have different distributions

204 of activation energy (de Caprariis et al. 2012; 2015). Their equations can be written  
 205 as:

$$206 \quad \begin{cases} \alpha = 1 - \int_0^{+\infty} \left( \exp \left( - \int_0^T \frac{A}{\beta} \exp \left( \frac{-E}{RT} \right) dT \right) \right) G(E) dE & n = 1 \quad (7) \\ \alpha = 1 - \int_0^{+\infty} (1 - n) \left( - \int_0^T \frac{A}{\beta} \exp \left( \frac{-E}{RT} \right) dT \right)^{\frac{1}{1-n}} G(E) dE & n \neq 1 \quad (8) \end{cases}$$

207 where

$$G(E) = \frac{\omega}{\sigma_1 \sqrt{2\pi}} \exp \left( \frac{-(E - E_1)^2}{2\sigma_1^2} \right) + \frac{1 - \omega}{\sigma_2 \sqrt{2\pi}} \exp \left( \frac{-(E - E_2)^2}{2\sigma_2^2} \right) \quad (9)$$

208 In the aforementioned equation,  $E$  is the activation energy,  $A$  is the pre-exponential  
 209 factor,  $R$  is the gas constant,  $\beta$  is the heating rate,  $n$  is the reaction order,  $T$  is the  
 210 absolute temperature,  $G(E)$  is the distribution of activation energies, and  $\omega$  is the  
 211 weighting factor ranging from 0 to 1 that describes the percentage of water that is  
 212 released during the primary or secondary dehydration steps.  $\omega = 1$  if all the water is  
 213 released during the first step, and  $\omega = 0$  if it is completely produced during the  
 214 secondary step.  $E_1$  and  $E_2$  are the mean activation energies of the first and second  
 215 reactions, respectively, and  $\sigma_1$  and  $\sigma_2$  are their standard deviations. In this equation,  
 216 the seven parameters to be estimated are  $n$ ,  $\omega$ ,  $E_1$ ,  $E_2$ ,  $\sigma_1$ ,  $\sigma_2$  and  $A$ .  $G(E)$  satisfies  
 217 the following condition:

$$\int_0^{+\infty} G(E) dE = 1 \quad (10)$$

218  $G(E)$  has many forms, such as a Gaussian, Weibull or Gamma distribution (Cai et al.  
 219 2014).

220 In the antigorite lattice (Uehara 1998), two different environments exist for OH  
 221 groups along the [010] axis (Capitani and Mellini 2004). Thus, the double-Gaussian

222 model (**Eq. 9**) is justified for  $G(E)$ . The O-H1 bond is surrounded by silica  
223 tetrahedrons (shown in blue in **Fig. 4**). We calculated the O-H bond lengths for  
224 antigorite using ab initio computational methods and found that the lengths of the  
225 O-H1 and O-H2 bonds are 0.970-0.971 Å and 0.974-0.981 Å, respectively. This result  
226 implies that the energies required to break these bonds are different, as shown by their  
227 different apparent activation energies upon dehydration.

228 In this work,  $n = 1$  was chosen, and  $A$  varied between  $10^8 \text{ s}^{-1}$  and  $10^{16} \text{ s}^{-1}$ .  
229 To explore antigorite dehydration, a simulated annealing algorithm (van Laarhoven  
230 and Aarts 1987) was used to determine  $\omega$ ,  $E_1$ ,  $E_2$ ,  $\sigma_1$ ,  $\sigma_2$  and  $A$ . Eq. 7 is  
231 numerically integrated with the inner integral computed using the Gaussian  
232 quadrature and the outer using the Romberg integral algorithm. An objective function  
233  $\Delta$  determines the accuracy of the six parameters. The lower the  $\Delta$ , the more accurate  
234 the six parameters. This function  $\Delta$  can be written as follows:

$$\Delta = \sum_{i=1}^M \sum_{j=1}^N (\alpha_{tij} - \alpha_{eij})^2 \quad (11)$$

235 where  $\alpha_{tij}$  is the  $\alpha$  value computed using Eq. 7 when the six parameters are  
236 known,  $\alpha_{eij}$  is the  $\alpha$  value measured via experiments,  $N$  is the number of data  
237 points in each heating rate, and  $M$  is the sum of the heating rates. The six parameters  
238 were determined using the simulated annealing algorithm and minimizing the  
239 objective function value.

240 As previously mentioned, the pre-exponential factor is shared by all the  
241 reactions in the adopted model. The pre-exponential factor is highly correlated with

242 the activation energy (Anthony et al. 1975; Du et al. 1991; Miura and Maki 1998),  
243 which leads to an unreliable value for the pre-exponential factor from the fit. This  
244 finding means that when the value of the pre-exponential factor is fitted together with  
245 the other parameters, non-unique values are typically found because of the  
246 compensation effect. In other words, different pairs of kinetic parameters provide an  
247 equally good fit to the experimental data. Thus, the pre-exponential factor must be  
248 fixed. We fixed the pre-exponential factor  $A$  within a range of  $10^8 - 10^{16} \text{ s}^{-1}$ , which  
249 is consistent with the transition-state theory (Várhegyi et al. 2011; Zhang et al. 2014)  
250 and yields the ranges of  $10^8 - 10^{12} \text{ s}^{-1}$ ,  $10^8 - 10^{13} \text{ s}^{-1}$ ,  $10^8 - 10^{14} \text{ s}^{-1}$ ,  
251  $10^8 - 10^{15} \text{ s}^{-1}$ , and  $10^8 - 10^{16} \text{ s}^{-1}$  for the pre-exponential factor, resulting from  
252 the simulated annealing algorithm searching in some ranges. The six parameters can  
253 be obtained using the simulated annealing algorithm when the pre-exponential factor  
254 is within a fixed range and  $n = 1$ . The fitting parameters are listed in **Table 2**.  $\log(A)$   
255 is linearly correlated with the average activation energies (**Fig. 5**);  $\log(A)$  increases  
256 with increasing activation energy. The correlation coefficients between  $\log(A)$  and the  
257 average activation energies ( $E_1$  and  $E_2$ ) are 0.9906 and 0.9986, respectively, which  
258 are very high values as expected. As shown in **Fig. 5**, multiple and interrelated values  
259 of the kinetic parameters are allowed by the fitting algorithm. The higher the  $A$  value,  
260 the higher the average activation energy. We show a clear relationship between the  
261 pre-exponential factor and the average activation energy, termed the compensation  
262 effect.

263 Since the atomic vibration frequency is typically on the order of  $\sim 10^{13} \text{ Hz}$ , it is

264 reasonable to fix the pre-exponential factor on the order of  $\sim 10^{13} \text{ s}^{-1}$ . We adopted the  
265 fitting parameters (**Table 2**) to obtain the dehydration kinetics when the  
266 pre-exponential factor is fixed on the order of  $\sim 10^{13} \text{ s}^{-1}$ . Using these fitting  
267 parameters, we calculate the reaction progress at different heating rates and show  
268 comparisons with the experimental data as shown in **Fig. 6**. It seems that the 2-DAEM  
269 works well with a very small  $\Delta = 0.031$  and a correlation coefficient of 0.999  
270 between the experimental data and the fitting results. Such a good fit of the  
271 experimental results means that the kinetics of antigorite dehydration are well  
272 modeled via 2-DEAM.

273 Processes  $G_1$  and  $G_2$  are referred to as the slow and the fast steps of  
274 dehydration, respectively. The structure of the antigorite crystal lattice (**Fig. 4**)  
275 contains two different local environments for OH groups, and the O-H1 and O-H2  
276 bonds have different lengths. In addition, the O-H3 bond is located at the boundary  
277 between the O-H1 and O-H2 bonds. Thus, the O-H3 bond is expected to show  
278 transitional behavior. The O-H1 bonds characterize 25.0% of the total OH groups;  
279 considering the O-H3 bonds as O-H1 bonds, their fraction reaches 34.4%. The  
280 weighting factor  $\omega$  (**Eq. 7**) is equal to 0.336, which is between 25% and 34.4%,  
281 implying that the O-H3 bond breaks during the transition between the slow and fast  
282 steps.

283 To explain antigorite dehydration kinetics, two sets of parallel dehydration  
284 reaction models are illustrated in **2-DAEM**. In our model, parallel dehydration  
285 reactions including a slow and fast mechanism occur at the same time. The weighting

286 factor  $\omega$  is 0.336, indicating that the fast step is dominant during the dehydration  
287 processes. In a previous study, the dehydration kinetics were investigated using  
288 time-resolved synchrotron X-ray diffraction in a closed system, showing that the  
289 dehydration occurs during two steps (Chollet et al. 2011), which impacts the  
290 seismicity (Ferrand et al. 2017).

291 During the first step (Chollet et al. 2011), according to backscattered electron images,  
292 only ~35% of the antigorite produces olivine and talc-like (intermediate hydrous  
293 phase; Perrillat et al. 2005), which is consistent with the weighting factor of 0.336 in  
294 the present study.

295 The probability densities of the  $G_1$  and  $G_2$  processes are plotted as a function  
296 of  $E$  (**Fig. 7**). The whole process follows a continuous distribution function. The  
297 activation energies that correspond to the slow step of antigorite dehydration ( $E_1$ ) are  
298 widely distributed, yielding a mean activation energy of  $268.1 \text{ kJ} \cdot \text{mol}^{-1}$ , while the  
299 energies corresponding to the fast step ( $E_2$ ) are in a narrow area and have much higher  
300 values, yielding a mean activation energy of  $299.2 \text{ kJ} \cdot \text{mol}^{-1}$ .

301 Recently, Sawai et al. (2013) studied antigorite dehydration using in situ  
302 high-temperature infrared microspectroscopy under isothermal conditions and found  
303 that the activation energies were  $219 \text{ kJ} \cdot \text{mol}^{-1}$  for bond 1,  $243 \text{ kJ} \cdot \text{mol}^{-1}$  for bond  
304 2, and  $256 \text{ kJ} \cdot \text{mol}^{-1}$  for bond 3. These authors concluded that antigorite  
305 dehydration occurred via one-dimensional diffusion. Gualtieri et al. (2012) conducted  
306 in situ X-ray powder diffraction to study antigorite dehydration kinetics and combined  
307 the results with transmission electron microscopy observations. These authors showed

308 that the apparent activation energy of antigorite dehydration within a temperature  
309 range of 885-981 K was  $255 \text{ kJ} \cdot \text{mol}^{-1}$ . Weber and Greer (1965) obtained an  
310 activation energy of 443-643  $\text{kJ} \cdot \text{mol}^{-1}$  using the Arrhenius equation and the  
311 relationship between the rate of reaction and the concentration. Our average activation  
312 energies ( $268.1 \text{ kJ} \cdot \text{mol}^{-1}$  and  $299.2 \text{ kJ} \cdot \text{mol}^{-1}$ ) obtained from 2-DAEM are higher  
313 than those reported by both Sawai et al. (2013) and Gualtieri et al. (2012) but lower  
314 than those ( $443\text{-}643 \text{ kJ} \cdot \text{mol}^{-1}$ ) reported by Weber and Greer (1965). In addition, the  
315 activation energy from Weber and Greer (1965) is higher than the maximum value of  
316  $400 \text{ kJ} \cdot \text{mol}^{-1}$  obtained from the FWO method in this study. In our model, the  
317 pre-exponential factor may explain that the different activation energies as  $\log(A)$  are  
318 linearly correlated with the activation energy (**Fig. 5**). The pre-exponential factor may  
319 cause substantial changes to the absolute value of the activation energy.

320

## 321 **Geophysical implications**

322 In many subduction zones, double seismic zones (DSZ) where earthquakes  
323 occur at different depths have been revealed. Intermediate-depth earthquakes occur  
324 along two dipping planes, that is, an upper plane and a lower plane (Hasegawa et al.  
325 1978). The hypothesis of a close link between earthquakes and dehydration events at  
326 intermediate depths has been proposed by many researchers (Chollet et al. 2011;  
327 Hilairet et al. 2007; Omori et al. 2004; Reynard 2013; Sawai et al. 2013) and is  
328 strongly supported by recent experimental results (Ferrand et al. 2017). The upper  
329 plane is likely related to the dehydration of metabasalts (e.g. Incel et al. 2017); the

330 seismicity of the lower plane in the subducting serpentinized mantle would be because  
331 of a dehydration-driven stress transfer from dehydrating antigorite along faults to  
332 fresh peridotite volumes (Ferrand et al. 2017). Whether peridotite embrittlement  
333 occurs or not depends on the competition between the dehydration kinetics and the  
334 solid matrix deformational rate. Dehydration kinetics are important parameters, and if  
335 they are faster than the rate of solid matrix deformation, seismic ruptures nucleate.

336         The fluid production rate is important, as a high rate may locally induce fluid  
337 overpressure along faults, which could explain the observed interplane seismicity  
338 (Kita and Katsumata 2015; Kita et al. 2010). The fluid production rate during  
339 antigorite dehydration is calculated from kinetic data. To determine the fluid  
340 production rate, we consider an isothermal model. Six parameters can be applied in  
341 the isothermal model to predict the dehydration rate of antigorite. In equation (7), we  
342 substitute  $\beta dt$  for  $dT$ ; thus, the isothermal model can be written as:

$$\begin{aligned} \alpha = 1 - \int_0^{+\infty} \exp\left(-\int_0^t A \exp\left(\frac{-E}{RT}\right) dt\right) \\ \times \left(\frac{\omega}{\sigma_1 \sqrt{2\pi}} \exp\left(\frac{-(E - E_1)^2}{2\sigma_1^2}\right) \right. \\ \left. + \frac{1 - \omega}{\sigma_2 \sqrt{2\pi}} \exp\left(\frac{-(E - E_2)^2}{2\sigma_2^2}\right)\right) dE \end{aligned} \quad (12)$$

343         We used the six parameters to compute the reaction progress ( $\alpha$ ) at different  
344 temperatures according to **Eq. 12**. The results are shown in **Fig. 8**. The antigorite  
345 dehydration rate increases with increasing temperature. In addition, at higher  
346 temperatures, the rate scarcely varies.



347 Dehydration rates ( $V_{1/2}$ ) can be obtained from the half-life time of the reaction  
348  $t_{1/2}$  when half of the antigorite has disappeared (Chollet et al. 2011).

$$V_{1/2} = \frac{C_{\text{H}_2\text{O}}}{t_{1/2}} \times \frac{\rho}{\rho_{\text{H}_2\text{O}}} \quad (13)$$

349 where  $t_{1/2}$  is the half-life time of the reaction when  $\alpha$  is equal to 0.5,  $C_{\text{H}_2\text{O}}$  is the  
350 water content of the mineral,  $\rho$  is its density  $2.62 \text{ g/cm}^3$  (Bezacier et al. 2010) and  
351  $\rho_{\text{H}_2\text{O}}$  is the density of water. The reaction progress ( $\alpha$ ) can be calculated with time  $t$   
352 at a given temperature  $T$ . The half-life time  $t_{1/2}$  can be obtained from the isothermal  
353 model as shown in **Fig. 8**. The fluid production rate  $V_{1/2}$  is  $8.0 \times 10^{-5}$ ,  $1.9 \times$   
354  $10^{-4}$ ,  $4.4 \times 10^{-4}$ ,  $9.8 \times 10^{-3}$ , and  $2.1 \times 10^{-3} m_{\text{fluid}}^3 m_{\text{rock}}^{-3} \text{ s}^{-1}$  for the temperatures  
355 of 893 K, 913 K, 933 K, 953 K, and 973 K, respectively, near the onset temperature of  
356 the isothermal dehydration reaction. This study strongly supports rapid dehydration,  
357 which is a key parameter for dehydration-induced seismicity. Sudden stress transfers  
358 are likely to occur in the vicinity of dehydrating serpentized faults, as recently  
359 demonstrated in laboratory analogs (Ferrand et al. 2017). These rates are faster than  
360 the viscous relaxation of antigorite ( $3 \times 10^{-7}$  to  $3 \times 10^{-12} \text{ s}^{-1}$ ) reported by Hilairet  
361 et al. (2007), indicating that antigorite dehydration leads to increased strain  
362 localization that is likely to induce mechanical instabilities in serpentized peridotites.  
363 Previous studies also have shown similar results. Chollet et al. (2011) measured the  
364 kinetics of antigorite dehydration in situ under high-temperature and high-pressure  
365 conditions using X-ray diffraction in a closed system and determined that the release  
366 of aqueous fluid occurs at  $10^{-4} m_{\text{fluid}}^3 m_{\text{rock}}^{-3} \text{ s}^{-1}$ . Perrillat et al. (2005) found that the  
367 discharge rate is on the order of  $10^{-6}$  to  $10^{-8} m_{\text{fluid}}^3 m_{\text{rock}}^{-3} \text{ s}^{-1}$  using a real-time

368 X-ray diffraction study. Previous studies have indicated that pressure has no  
369 significant effect on kinetics (Perrillat et al. 2005; Rubie and Thompson 1985);  
370 therefore, our results under a condition of ambient pressure can be extrapolated to  
371 subduction zones. By combining previous results (Chollet et al. 2011; Hilairet et al.  
372 2007; Perrillat et al. 2005; Sawai et al. 2013) and those of this study, we found that  
373 antigorite dehydration rates are higher than the characteristic relaxation, which is  
374 calculated as the inverse of the Maxwell relaxation time, and that brittle failure is  
375 likely to occur within dehydrating serpentinized peridotites. Therefore, as described  
376 by the dehydration-driven stress transfer model (Ferrand et al. 2017), antigorite  
377 dehydration may trigger seismicity in the lower plane of the double seismic zone.

378

379

380

381

## 382 **References**

383

384 Abers, G.A., Nakajima, J., van Keken, P.E., Kita, S., and Hacker, B.R. (2013) Thermal–  
385 petrological controls on the location of earthquakes within subducting plates. *Earth  
386 and Planetary Science Letters*, 369-370, 178-187.

387 Anthony, D.B., Howard, J.B., Hottel, H.C., and Meissner, H.P. (1975) Rapid devolatilization of  
388 pulverized coal. *Symposium (International) on Combustion*, 15(1), 1303-1317.

389 Balucan, R.D., Kennedy, E.M., Mackie, J.F., and Dlugogorski, B.Z. (2011) Optimization of

- 390 antigorite heat pre-treatment via kinetic modeling of the dehydroxylation reaction for  
391 CO<sub>2</sub> mineralization. *Greenhouse Gases: Science and Technology*, 1(4), 294-304.
- 392 Bezacier, L., Reynard, B., Bass, J.D., Sanchez-Valle, C., and Van de Moortèle, B. (2010)  
393 Elasticity of antigorite, seismic detection of serpentinites, and anisotropy in subduction  
394 zones. *Earth and Planetary Science Letters*, 289(1), 198-208.
- 395 Cai, J., Wu, W., and Liu, R. (2014) An overview of distributed activation energy model and its  
396 application in the pyrolysis of lignocellulosic biomass. *Renewable and Sustainable  
397 Energy Reviews*, 36(Supplement C), 236-246.
- 398 Capitani, G., and Mellini, M. (2004) The modulated crystal structure of antigorite: The  $m = 17$   
399 polysome. *American Mineralogist*, 89(1), 147-158.
- 400 Chernak, L.J., and Hirth, G. (2010) Deformation of antigorite serpentinite at high temperature  
401 and pressure. *Earth and Planetary Science Letters*, 296(1), 23-33.
- 402 Chernak, L.J., and Hirth, G. (2011) Syndeformational antigorite dehydration produces stable  
403 fault slip. *Geology*, 39(9), 847-850.
- 404 Chollet, M., Daniel, I., Koga, K.T., Morard, G., and van de Moortèle, B. (2011) Kinetics and  
405 mechanism of antigorite dehydration: Implications for subduction zone seismicity.  
406 *Journal of Geophysical Research: Solid Earth*, 116(B4), n/a-n/a.
- 407 Clark, S.J. (2005) First principles methods using CASTEP. *Z. Kristallogr.*, 220, 567-570.
- 408 de Caprariis, B., De Filippis, P., Herce, C., and Verdone, N. (2012) Double-Gaussian  
409 Distributed Activation Energy Model for Coal Devolatilization. *Energy & Fuels*, 26(10),  
410 6153-6159.
- 411 de Caprariis, B., Santarelli, M.L., Scarsella, M., Herce, C., Verdone, N., and De Filippis, P.

- 412 (2015) Kinetic analysis of biomass pyrolysis using a double distributed activation  
413 energy model. *Journal of Thermal Analysis and Calorimetry*, 121(3), 1403-1410.
- 414 Dobson, D.P., Meredith, P.G., and Boon, S.A. (2002) Simulation of Subduction Zone  
415 Seismicity by Dehydration of Serpentine. *Science*, 298(5597), 1407-1410.
- 416 Du, Z., F. Sarofim, A., P. Longwell, J., and Mims, C. (1991) Kinetic measurement and  
417 modeling of carbon oxidation. *Energy & Fuels*, 5(1), 214-221.
- 418 Egger, D.H., and Ehmann, A.N. (2010) Rate of antigorite dehydration at 2 GPa applied to  
419 subduction zones. *American Mineralogist*, 95(5-6), 761-769.
- 420 Ferrand, T.P., Hilaret, N., Incel, S., Deldicque, D., Labrousse, L., Gasc, J., Renner, J., Wang,  
421 Y., Green li, H.W., and Schubnel, A. (2017) Dehydration-driven stress transfer triggers  
422 intermediate-depth earthquakes. *Nature Communications*, 8, 15247.
- 423 Ferrand, T.P., Labrousse, L., Eloy, G., Fabbri, O., Hilaret, N., and Schubnel, A. (2018) Energy  
424 Balance From a Mantle Pseudotachylyte, Balmuccia, Italy. *Journal of Geophysical  
425 Research: Solid Earth*, 123(5), 3943-3967.
- 426 Flynn, J.H., and Wall, L.A. (1967) Initial kinetic parameters from thermogravimetric rate and  
427 conversion data. *Journal of Polymer Science Part B: Polymer Letters*, 5(2), 191-196.
- 428 Gasc, J., Hilaret, N., Yu, T., Ferrand, T., Schubnel, A., and Wang, Y. (2017) Faulting of natural  
429 serpentinite: Implications for intermediate-depth seismicity. *Earth and Planetary  
430 Science Letters*, 474, 138-147.
- 431 Gasc, J., Schubnel, A., Brunet, F., Guillon, S., Mueller, H.-J., and Lathe, C. (2011)  
432 Simultaneous acoustic emissions monitoring and synchrotron X-ray diffraction at high  
433 pressure and temperature: Calibration and application to serpentinite dehydration.

- 434 Physics of the Earth and Planetary Interiors, 189(3), 121-133.
- 435 Gualtieri, A.F., Giacobbe, C., and Viti, C. (2012) The dehydroxylation of serpentine group  
436 minerals. American Mineralogist, 97(4), 666-680.
- 437 Hacker, B.R., Peacock, S.M., Abers, G.A., and Holloway, S.D. (2003) Subduction factory 2.  
438 Are intermediate-depth earthquakes in subducting slabs linked to metamorphic  
439 dehydration reactions? Journal of Geophysical Research: Solid Earth, 108(B1),  
440 n/a-n/a.
- 441 Hamann, D.R., Schlüter, M., and Chiang, C. (1979) Norm-Conserving Pseudopotentials.  
442 Physical Review Letters, 43(20), 1494-1497.
- 443 Hasegawa, A., Umino, N., and Takagi, A. (1978) Double-planed structure of the deep seismic  
444 zone in the northeastern Japan arc. Tectonophysics, 47(1), 43-58.
- 445 Hattori, K., and Guillot, S. (2003) Volcanic fronts form as a consequence of serpentinite  
446 dehydration in the forearc mantle wedge. Geology, 31(6), 525-528.
- 447 Hilairet, N., Reynard, B., Wang, Y., Daniel, I., Merkel, S., Nishiyama, N., and Petitgirard, S.  
448 (2007) High-Pressure Creep of Serpentine, Interseismic Deformation, and Initiation of  
449 Subduction. Science, 318(5858), 1910-1913.
- 450 Hyndman, R.D., and Peacock, S.M. (2003) Serpentinization of the forearc mantle. Earth and  
451 Planetary Science Letters, 212(3), 417-432.
- 452 Incel, S., Hilairet, N., Labrousse, L., John, T., Deldicque, D., Ferrand, T., Wang, Y., Renner, J.,  
453 Morales, L., and Schubnel, A. (2017) Laboratory earthquakes triggered during  
454 eclogitization of lawsonite-bearing blueschist. Earth and Planetary Science Letters,  
455 459, 320-331.

- 456 Jung, H., Green li, H.W., and Dobrzhinetskaya, L.F. (2004) Intermediate-depth earthquake  
457 faulting by dehydration embrittlement with negative volume change. *Nature*, 428, 545.
- 458 Kita, S., and Katsumata, K. (2015) Stress drops for intermediate-depth intraslab earthquakes  
459 beneath Hokkaido, northern Japan: Differences between the subducting oceanic crust  
460 and mantle events. *Geochemistry, Geophysics, Geosystems*, 16(2), 552-562.
- 461 Kita, S., Okada, T., Hasegawa, A., Nakajima, J., and Matsuzawa, T. (2010) Existence of  
462 interplane earthquakes and neutral stress boundary between the upper and lower  
463 planes of the double seismic zone beneath Tohoku and Hokkaido, northeastern Japan.  
464 *Tectonophysics*, 496(1), 68-82.
- 465 Lin, J.S., Qteish, A., Payne, M.C., and Heine, V. (1993) Optimized and transferable nonlocal  
466 separable ab initio pseudopotentials. *Physical Review B*, 47(8), 4174-4180.
- 467 Mellini, M., Trommsdorff, V., and Compagnoni, R. (1987) Antigorite polysomatism: behaviour  
468 during progressive metamorphism. *Contributions to Mineralogy and Petrology*, 97(2),  
469 147-155.
- 470 Miura, K., and Maki, T. (1998) A Simple Method for Estimating  $f(E)$  and  $k_0(E)$  in the Distributed  
471 Activation Energy Model. *Energy & Fuels*, 12(5), 864-869.
- 472 Navarro, M.V., Aranda, A., Garcia, T., Murillo, R., and Mastral, A.M. (2008) Application of the  
473 distributed activation energy model to blends devolatilisation. *Chemical Engineering  
474 Journal*, 142(1), 87-94.
- 475 Okazaki, K., and Hirth, G. (2016) Dehydration of lawsonite could directly trigger earthquakes in  
476 subducting oceanic crust. *Nature*, 530, 81-84.
- 477 Omori, S., Komabayashi, T., and Maruyama, S. (2004) Dehydration and earthquakes in the

- 478 subducting slab: empirical link in intermediate and deep seismic zones. *Physics of the*  
479 *Earth and Planetary Interiors*, 146(1), 297-311.
- 480 Ozawa, T. (1965) A New Method of Analyzing Thermogravimetric Data. *Bulletin of the*  
481 *Chemical Society of Japan*, 38(11), 1881-1886.
- 482 Ozawa, T. (1970) Kinetic analysis of derivative curves in thermal analysis. *Journal of Thermal*  
483 *Analysis and Calorimetry*, 2(3), 301-324.
- 484 Ozawa, T. (1986) Non-isothermal kinetics and generalized time. *Thermochimica Acta*, 100(1),  
485 109-118.
- 486 Peacock, S.M. (2001) Are the lower planes of double seismic zones caused by serpentine  
487 dehydration in abducting oceanic mantle? *Geology*, 29(4), 299-302.
- 488 Peacock, S.M., and Wang, K. (1999) Seismic Consequences of Warm Versus Cool  
489 Subduction Metamorphism: Examples from Southwest and Northeast Japan. *Science*,  
490 286(5441), 937-939.
- 491 Pérez-Rodríguez, J.L., Franco, F., Ramírez-Valle, V., and Pérez-Maqueda, L.A. (2005)  
492 Modification of the thermal dehydroxylation of antigorite by ultrasound treatment.  
493 *Journal of Thermal Analysis and Calorimetry*, 82(3), 769-774.
- 494 Perrillat, J.-P., Daniel, I., Koga, K.T., Reynard, B., Cardon, H., and Crichton, W.A. (2005)  
495 Kinetics of antigorite dehydration: A real-time X-ray diffraction study. *Earth and*  
496 *Planetary Science Letters*, 236(3), 899-913.
- 497 Plümpner, O., John, T., Podladchikov, Y.Y., Vrijmoed, J.C., and Scambelluri, M. (2016) Fluid  
498 escape from subduction zones controlled by channel-forming reactive porosity. *Nature*  
499 *Geoscience*, 10, 150.

- 500 Reynard, B. (2013) Serpentine in active subduction zones. *Lithos*, 178(Supplement C),  
501 171-185.
- 502 Reynard, B., Hilairet, N., Balan, E., and Lazzeri, M. (2007) Elasticity of serpentines and  
503 extensive serpentinization in subduction zones. *Geophysical Research Letters*, 34(13),  
504 n/a-n/a.
- 505 Rubie, D.C., and Thompson, A.B. (1985) Kinetics of Metamorphic Reactions at Elevated  
506 Temperatures and Pressures: An Appraisal of Available Experimental Data. In A.B.  
507 Thompson, and D.C. Rubie, Eds. *Metamorphic Reactions: Kinetics, Textures, and*  
508 *Deformation*, p. 27-79. Springer New York, New York, NY.
- 509 Sawai, M., Katayama, I., Hamada, A., Maeda, M., and Nakashima, S. (2013) Dehydration  
510 kinetics of antigorite using in situ high-temperature infrared microspectroscopy.  
511 *Physics and Chemistry of Minerals*, 40(4), 319-330.
- 512 Scambelluri, M., Bottazzi, P., Trommsdorff, V., Vannucci, R., Hermann, J., Gómez-Pugnaire,  
513 M.T., and López-Sánchez Vizcaino, V. (2001) Incompatible element-rich fluids  
514 released by antigorite breakdown in deeply subducted mantle. *Earth and Planetary*  
515 *Science Letters*, 192(3), 457-470.
- 516 Scambelluri, M., Pennacchioni, G., Gilio, M., Bestmann, M., Plümper, O., and Nestola, F.  
517 (2017) Fossil intermediate-depth earthquakes in subducting slabs linked to differential  
518 stress release. *Nature Geoscience*, 10(12), 960-966.
- 519 Schmidt, M.W., and Poli, S. (1998) Experimentally based water budgets for dehydrating slabs  
520 and consequences for arc magma generation. *Earth and Planetary Science Letters*,  
521 163(1), 361-379.



- 522 Shao, T., Ji, S., Kondo, Y., Michibayashi, K., Wang, Q., Xu, Z., Sun, S., Marcotte, D., and  
523 Salisbury, M.H. (2014) Antigorite-induced seismic anisotropy and implications for  
524 deformation in subduction zones and the Tibetan Plateau. *Journal of Geophysical*  
525 *Research: Solid Earth*, 119(3), 2068-2099.
- 526 Soyer, W., and Unsworth, M. (2006) Deep electrical structure of the northern Cascadia (British  
527 Columbia, Canada) subduction zone: Implications for the distribution of fluids.  
528 *Geology*, 34(1), 53-56.
- 529 Trittschack, R., and Grob ty, B. (2012) Dehydroxylation kinetics of lizardite. *European Journal*  
530 *of Mineralogy*, 24(1), 47-57.
- 531 Uehara, S. (1998) TEM and XRD study of antigorite superstructures. *The Canadian*  
532 *Mineralogist*, 36(6), 1595-1605.
- 533 Ulmer, P., and Trommsdorff, V. (1995) Serpentine Stability to Mantle Depths and  
534 Subduction-Related Magmatism. *Science*, 268(5212), 858-861.
- 535 van Laarhoven, P.J.M., and Aarts, E.H.L. (1987) Simulated annealing. In P.J.M. van  
536 Laarhoven, and E.H.L. Aarts, Eds. *Simulated Annealing: Theory and Applications*, p.  
537 7-15. Springer Netherlands, Dordrecht.
- 538 V rhegyi, G., Bob ly, B., Jakab, E., and Chen, H. (2011) Thermogravimetric Study of Biomass  
539 Pyrolysis Kinetics. A Distributed Activation Energy Model with Prediction Tests.  
540 *Energy & Fuels*, 25(1), 24-32.
- 541 Viti, C. (2010) Serpentine minerals discrimination by thermal analysis. *American Mineralogist*,  
542 95(4), 631-638.
- 543 Vyazovkin, S., and Wight, C.A. (1997) KINETICS IN SOLIDS. *Annual Review of Physical*

- 544 Chemistry, 48(1), 125-149.
- 545 Wang, D., Liu, X., Liu, T., Shen, K., Welch, D.O., and Li, B. (2017) Constraints from the  
546 dehydration of antigorite on high-conductivity anomalies in subduction zones.  
547 Scientific Reports, 7(1), 16893.
- 548 Wang, D., Wang, Y., Yi, L., and Huang, B. (2015) Dehydration Kinetics of Natural Talc. The  
549 Canadian Mineralogist, 53(4), 643-651.
- 550 Weber, J.N., and Greer, R.T. (1965) Dehydration of serpentine: Heat of reaction and reaction  
551 kinetics at  $P_{H_2O} = 1$  atm. The American Mineralogist, 50, 450-464.
- 552 Worzewski, T., Jegen, M., Kopp, H., Brasse, H., and Taylor Castillo, W. (2010) Magnetotelluric  
553 image of the fluid cycle in the Costa Rican subduction zone. Nature Geoscience, 4,  
554 108.
- 555 Yamasaki, T., and Seno, T. (2003) Double seismic zone and dehydration embrittlement of the  
556 subducting slab. Journal of Geophysical Research: Solid Earth, 108(B4), n/a-n/a.
- 557 Zhang, J., Chen, T., Wu, J., and Wu, J. (2014) Multi-Gaussian-DAEM-reaction model for  
558 thermal decompositions of cellulose, hemicellulose and lignin: Comparison of  $N_2$  and  
559  $CO_2$  atmosphere. Bioresource Technology, 166(Supplement C), 87-95.

560

561

562

563 **Acknowledgements.** We thank Ikuo Katayama for his kindly providing the natural  
564 antigorite rock sample. We also thank Wen Wen for technical assistance during the  
565 X-ray diffraction in situ high temperature experiments at BL14B1 of the Shanghai  
566 Synchrotron Radiation Facility. This study was partially supported by the Natural  
567 Science Foundation of China (Grant No. 41874104, 41373060 and 41603061) and the  
568 CAS/CAFEA International Partnership Program for Creative Research Teams (No.

569 KZZD-EW- TZ-19). Careful reviews by Thomas P. Ferrand and an anonymous  
570 reviewer helped to improve the manuscript. We thank Callum Hetherington for  
571 editorial handling.

572

573

574

575

576

577

578

579

580

581

582

583

584

585

586

587

588

589

590

591

592

593

594

595

596

597

598

599

600

601

602

603

604

605

606

607

608 **Table 1 Kinetic triplet and errors obtained using an  $n$ -th order reaction**

609

SSA ( $s^{-1}$ )	$A$ ( $s^{-1}$ )	$n$	$E$ ( $\text{kJ} \cdot \text{mol}^{-1}$ )	$\Delta$
$10^8 \sim 10^{12}$	$(3.44 \pm 0.17) \times 10^9$	$2.2 \pm 0.1$	$212.2 \pm 10.6$	0.22

$10^8 \sim 10^{13}$	$(6.41 \pm 0.32) \times 10^9$	$2.2 \pm 0.1$	$217.3 \pm 10.9$	0.23
$10^8 \sim 10^{14}$	$(4.54 \pm 0.23) \times 10^9$	$2.2 \pm 0.1$	$215.6 \pm 10.8$	0.24

610  
 611  
 612  
 613  
 614  
 615  
 616  
 617  
 618  
 619  
 620  
 621  
 622  
 623  
 624  
 625  
 626  
 627  
 628  
 629  
 630  
 631  
 632  
 633  
 634  
 635  
 636  
 637  
 638  
 639  
 640  
 641  
 642  
 643  
 644  
 645  
 646  
 647  
 648

SSA is the search space of  $A$  (SSA).  $A$ ,  $n$  and  $E$  are three constant parameters termed the kinetic triplet in the  $n$ -order model, which are determined from **Eq. 4** and **Eq. 6**.  $\Delta$  is an objective function, which was defined to describe the error between experimental and fitting data. The lower the  $\Delta$ , the more accurate the kinetic triplet.

**Table 2 Kinetic parameters and errors obtained using 2-DAEM**

SSA	$A$	$E_1$	$\sigma_1$	$E_2$	$\sigma_2$	$\omega$	$\Delta$
( $s^{-1}$ )	( $s^{-1}$ )	( $\text{kJ} \cdot \text{mol}^{-1}$ )	( $\text{kJ} \cdot \text{mol}^{-1}$ )	( $\text{kJ} \cdot \text{mol}^{-1}$ )	( $\text{kJ} \cdot \text{mol}^{-1}$ )		

$10^8 \sim 10^{12}$	$(1.58 \pm 0.16) \times 10^{11}$	227.0±4.5	28.0±5.6	251.4±5.0	3.1±0.2	0.336±0.017	0.040
$10^8 \sim 10^{13}$	$(2.08 \pm 0.21) \times 10^{12}$	249.7±5.0	34.6±6.9	272.2±5.4	4.8±0.2	0.336±0.017	0.033
$10^8 \sim 10^{14}$	$(4.66 \pm 0.47) \times 10^{13}$	268.1±5.4	29.8±6.0	299.2±6.0	8.9±0.5	0.336±0.017	0.031
$10^8 \sim 10^{15}$	$(4.42 \pm 0.44) \times 10^{14}$	298.2±6.0	37.6±7.5	312.3±6.2	10.4±0.5	0.336±0.017	0.030
$10^8 \sim 10^{16}$	$(3.97 \pm 0.40) \times 10^{15}$	307.1±6.1	44.4±8.9	330.9±6.6	8.6±0.4	0.336±0.017	0.029

649 SSA is the search space of  $A$ .  $A$ ,  $\omega$ ,  $E_i$ , and  $\sigma_i$  are the parameters determined from  
 650 **Eq. 7**.  $\Delta$  is an objective function to determine the accuracy of the six parameters.  
 651 The lower the  $\Delta$ , the more accurate the six parameters.

652  
 653  
 654  
 655  
 656  
 657  
 658  
 659  
 660  
 661  
 662  
 663  
 664  
 665  
 666  
 667  
 668  
 669  
 670  
 671  
 672  
 673  
 674  
 675  
 676  
 677  
 678  
 679  
 680  
 681  
 682  
 683

#### 684 **Figure captions**

685  
 686

687 **Figure 1 Reaction progress curves for antigorite with different heating rates.**

688

689 The red, green, blue and violet lines represent the reaction progress with heating rates  
690 of 10, 15, 20 and 25  $\text{K} \cdot \text{min}^{-1}$ , respectively. The numbers are the heating rates.

691

692

693 **Figure 2 Activation energy of antigorite as a function of the reaction progress**  
694 **determined using the FWO method.**

695

696 The FWO method is a model-free method for calculation of activation energy in TG  
697 (Eq. 5). FWO is Flynn-Wall-Ozawa.

698

699

700 **Figure 3 Experimental and theoretical reaction progress curves of the**  
701 **non-isothermal experiments for antigorite derived from the  $n$ -th order reaction.**

702

703 a, b, c and d represent the fitting results of 10, 15, 20, and 25  $\text{K} \cdot \text{min}^{-1}$  based on the  
704  $n$ -th order model, respectively. The red line and blue line represent the calculated data  
705 and experimental data, respectively, of  $\alpha$  as a function of temperature, with  
706  $A = 3.44 \times 10^9 \text{ s}^{-1}$ ;  $n = 2.2$  and  $E = 212.2 \text{ kJ} \cdot \text{mol}^{-1}$ .

707

708

709 **Figure 4 Structure of the antigorite crystal lattice, showing different local**  
710 **environments for OH groups.**

711

712 The red, blue, white and yellow balls represent oxygen, silicon, hydrogen and  
713 magnesium atoms, respectively. The structure of the antigorite crystal lattice (Capitani  
714 and Mellini 2004) contains two different local environments for OH groups, that is,  
715 O-H1 and O-H2. The O-H1 and O-H2 bonds have different lengths. The O-H3 bond is  
716 at the boundary between the O-H1 and O-H2 bonds. The lengths of O-H1 and O-H2  
717 bonds were determined using first-principle calculations.

718

719 **Figure 5 A compensation effect between the pre-exponential factor ( $A$ ) and the**  
720 **average activation energy based on 2-DAEM.**

721

722 Logarithm of pre-exponential factor ( $A$ ) as a function of activation energy ( $E_1$  and  $E_2$ )  
723 for antigorite dehydration. The red and blue squares represent data points for  $E_1$  and  
724  $E_2$

725 , respectively. The regression equations are  $\log(A) = 0.0527 \times E_1 - 0.7634$  and  
726  $\log(A) = 0.0559 \times E_2 - 2.9165$ . The correlation coefficients between  $\log(A)$  and the  
727 average activation energies ( $E_1$  and  $E_2$ ) are 0.9906 and 0.9986, respectively.

728

729

730 **Figure 6 Comparisons between the calculated data and experimental data of**  
731 **antigorite according to 2-DAEM.**

732

733 a, b, c and d represent the fitting results of 10, 15, 20, and 25 K · min<sup>-1</sup> based on  
734 2-DAEM, respectively. The red and blue lines represent the calculated and  
735 experimental data, respectively, of  $\alpha$  with temperature.  $\alpha$  was calculated according  
736 to **Eq. 7** at a given  $A$ ,  $E_i$ ,  $\sigma_i$  and  $\omega$  are listed in the third row in Table 2 when  $\Delta$   
737 has the minimum value of 0.014. The correlation coefficients for the heating rates of  
738 10, 15, 20, and 25 Kmin<sup>-1</sup> are, respectively, 0.9996, 0.9995, 0.9994 and 0.9991.

739

#### 740 **Figure 7 Distributions of the activation energies in 2-DAEM.**

741

742 The green, blue and red lines denote  $G_1(E)$ ,  $G_2(E)$  and  $G(E)$ , respectively, where

743  $G_1(E) = \frac{\omega}{\sigma_1\sqrt{2\pi}} \exp\left(\frac{-(E-E_1)^2}{2\sigma_1^2}\right)$  is the distribution of the activation energy under local

744 environments for the O-H1 bond and  $G_2(E) = \frac{1-\omega}{\sigma_2\sqrt{2\pi}} \exp\left(\frac{-(E-E_2)^2}{2\sigma_2^2}\right)$  is the

745 distribution of the activation energy under local environments for the O-H2 bond.

746  $G(E)$  is the sum of  $G_1(E)$  and  $G_2(E)$ .

747

#### 748 **Figure 8 Isothermal dehydration kinetic models for antigorite at different** 749 **temperatures derived from the parameters of the non-isothermal experiments.**

750

751 These curves show the calculated reaction progress at certain temperatures according  
752 to **Eq. 12**. The numbers are temperatures.  $\alpha$  was calculated according to **Eq. 12** at a  
753 given temperature with parameters  $A$ ,  $E_i$  and  $\sigma_i$  chosen from the third row of Table 2.

754

755

756

757

758

759

760

Fig. 1

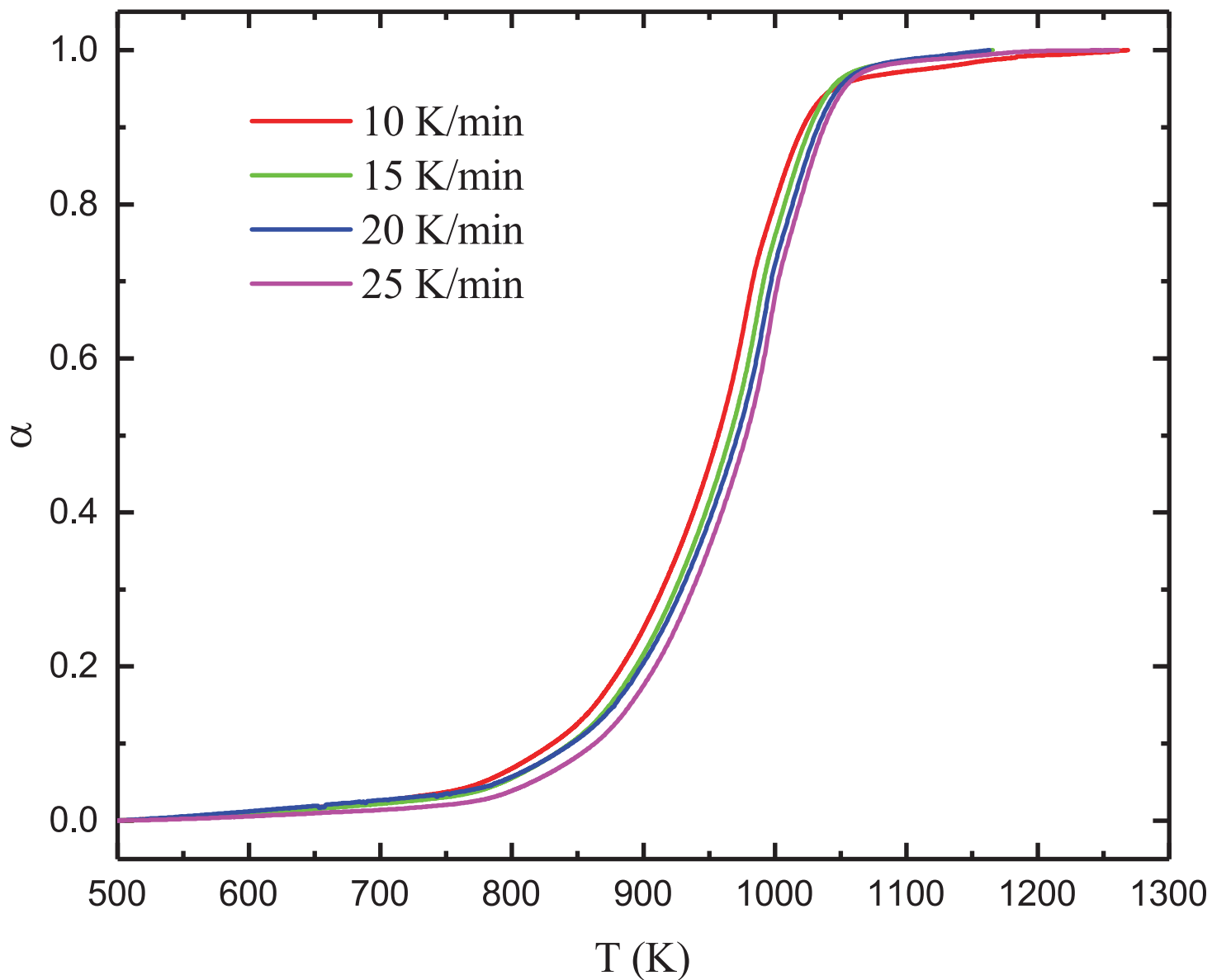




Fig. 2

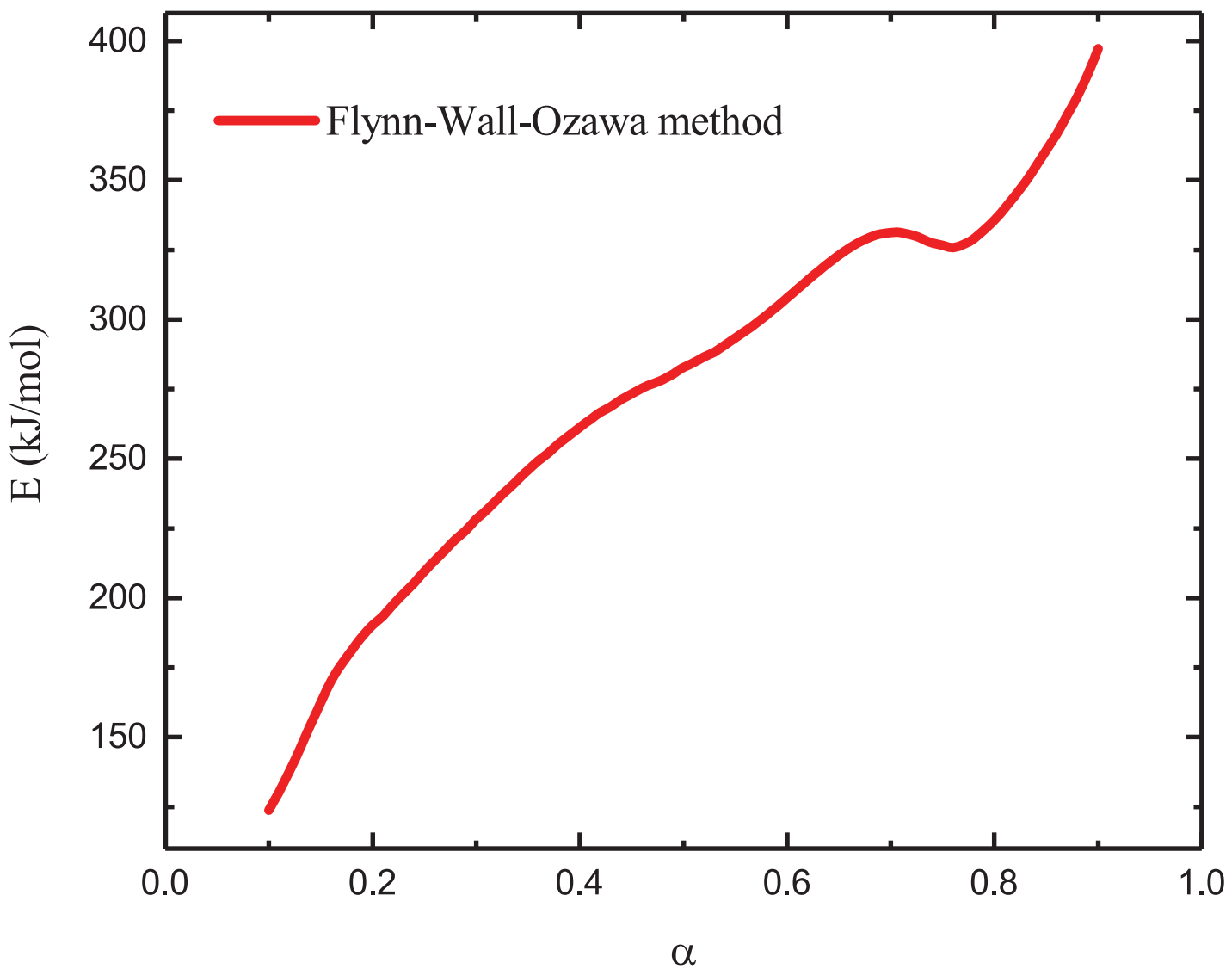


Fig. 3

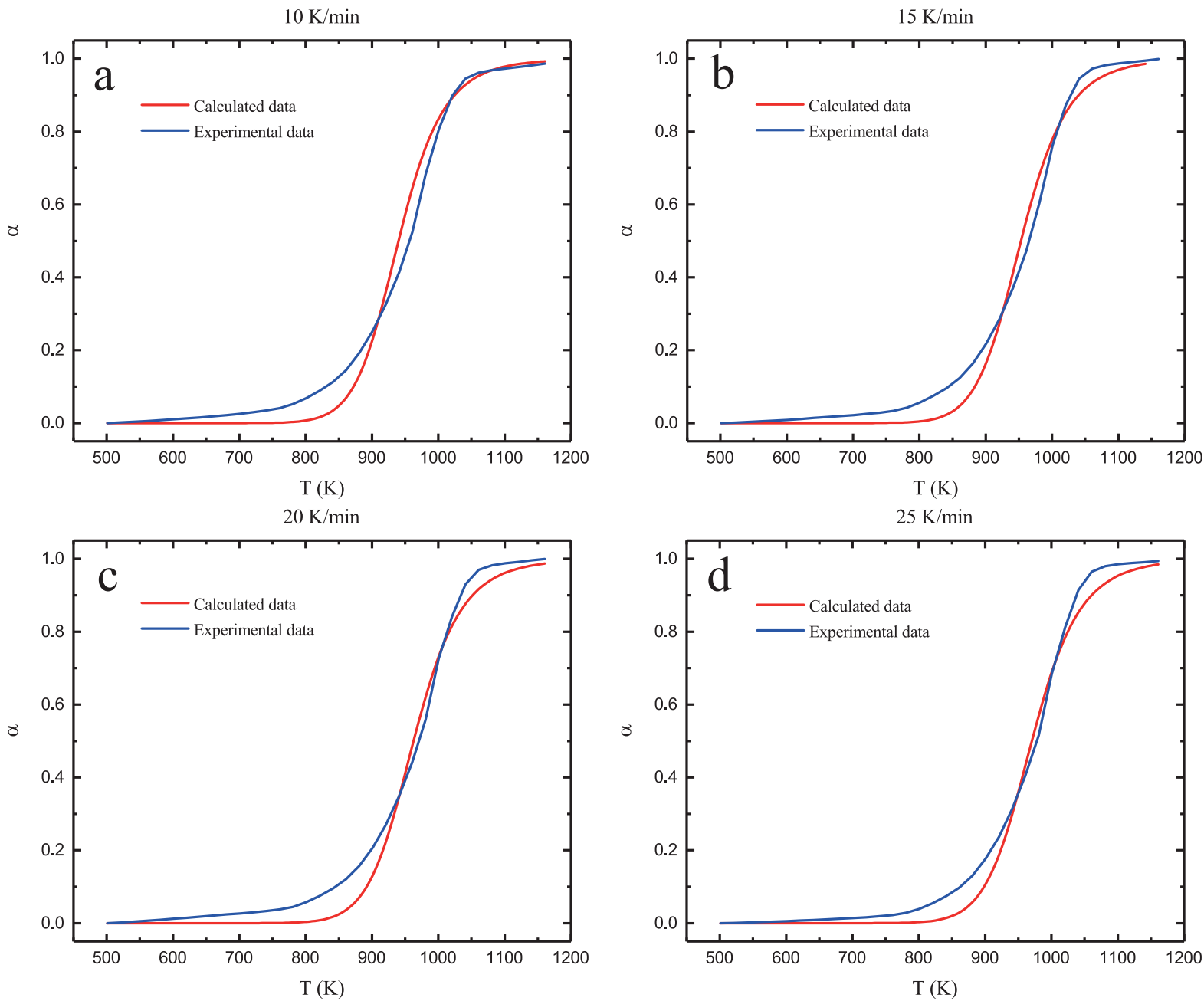


Fig. 4

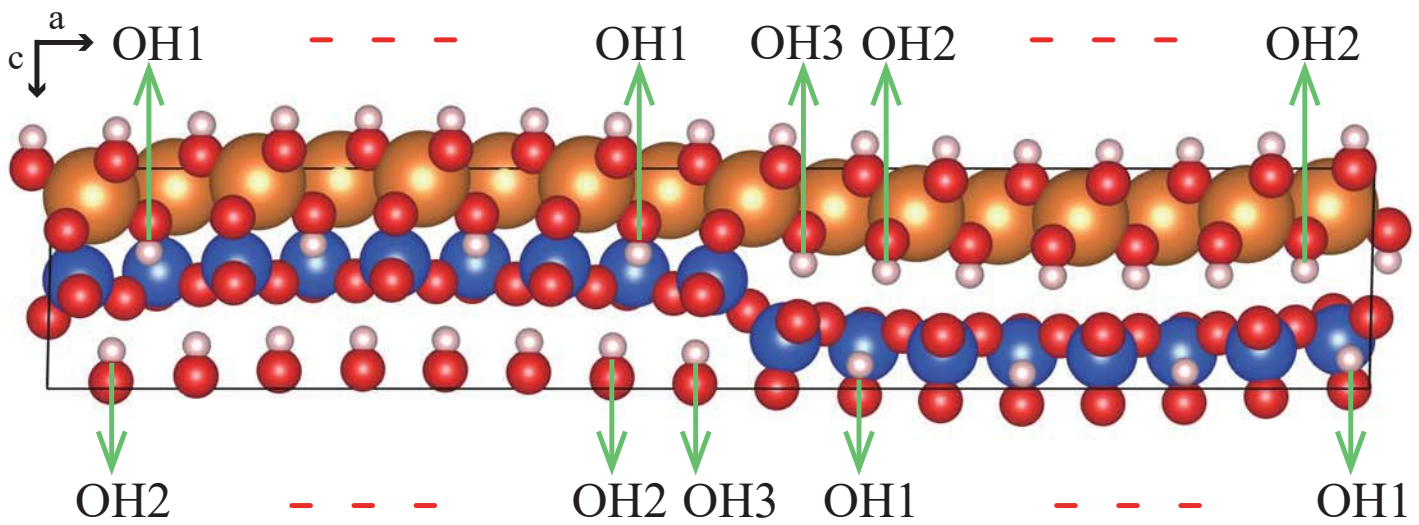


Fig. 5

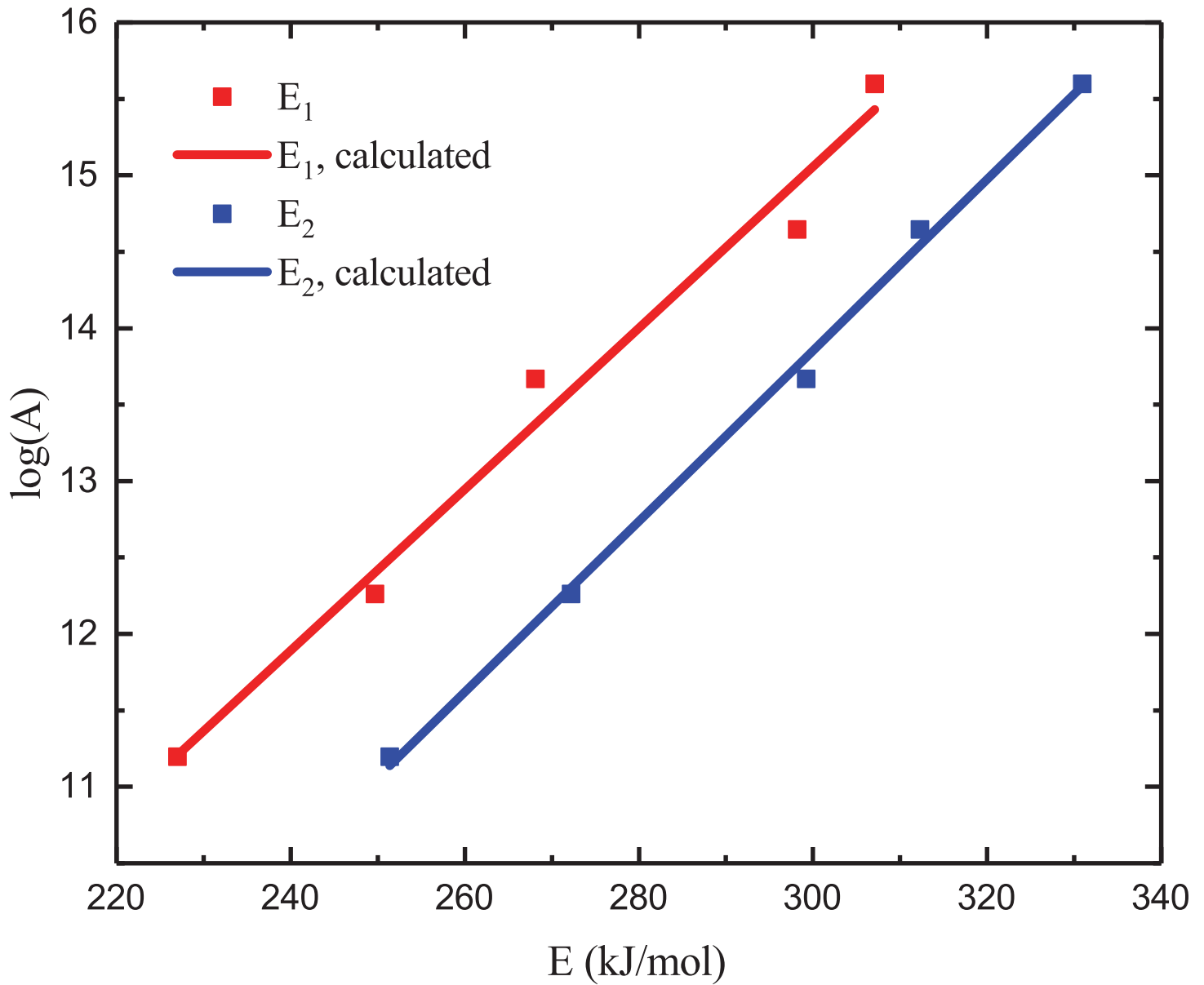


Fig. 6

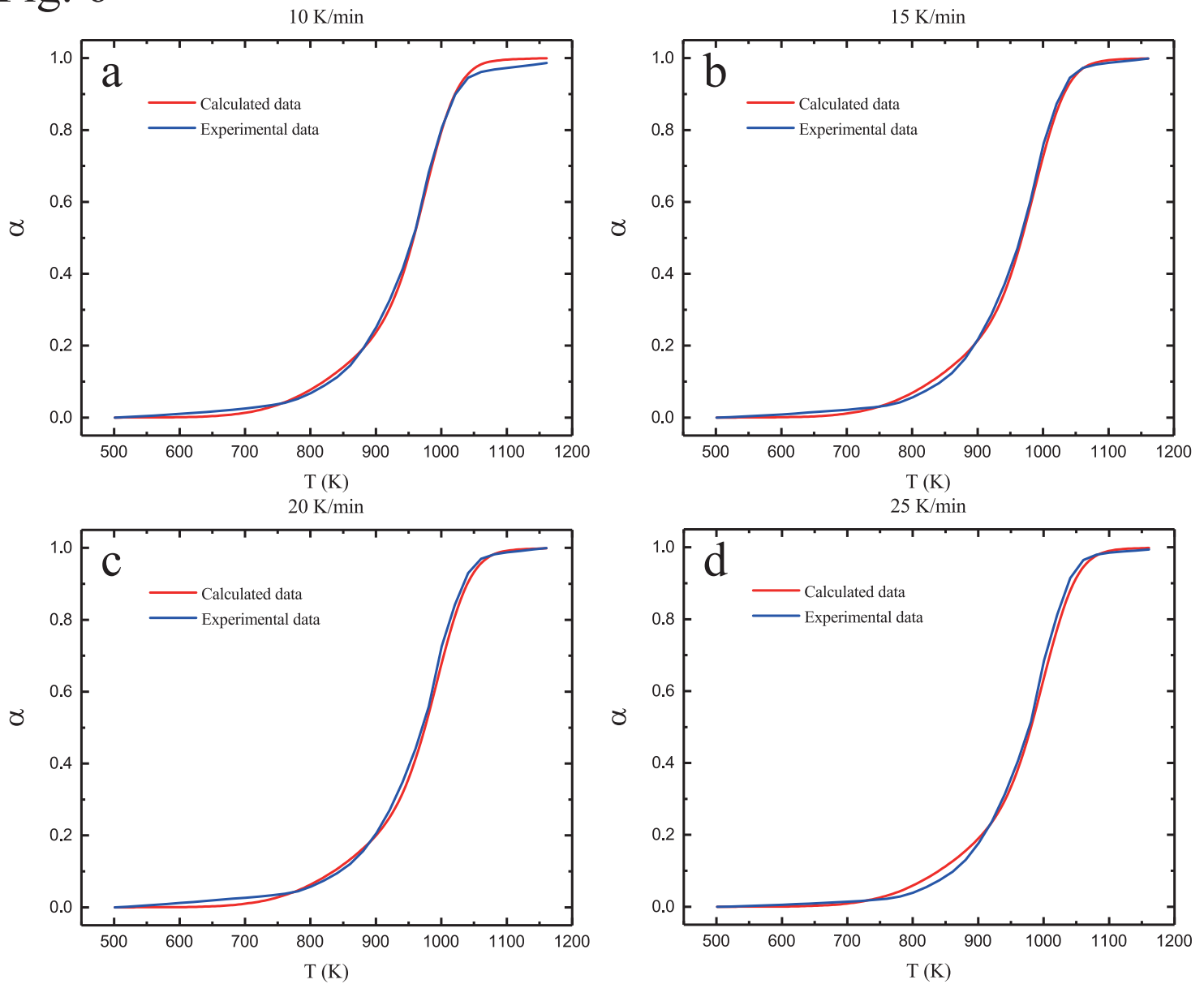


Fig. 7

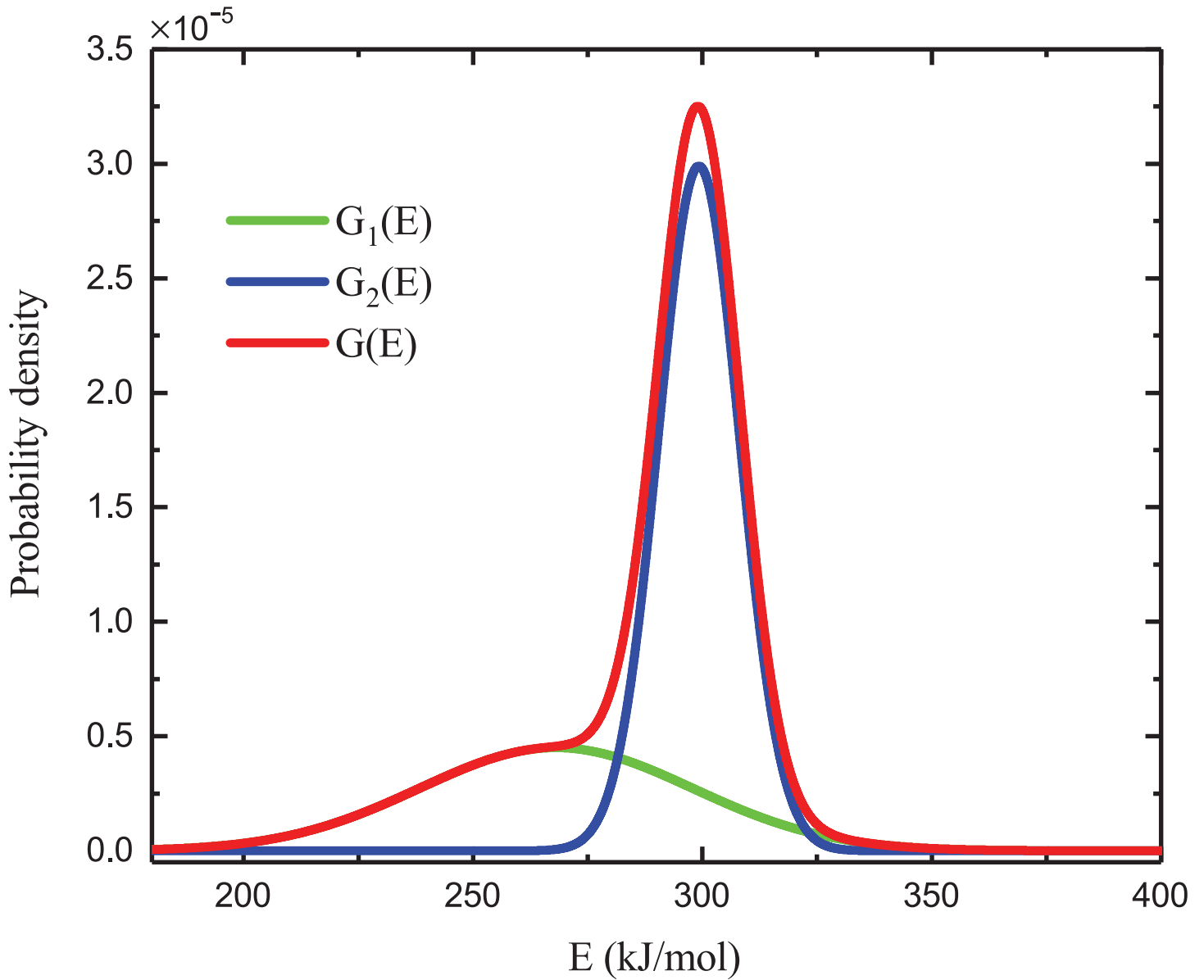


Fig. 8

